Supporting Information:

Whisky Tasting using a Bimetallic Nanoplasmonic Tongue

Gerard Macias‡ [a], *Justin R. Sperling‡* [a], *William J. Peveler* [b], *Glenn A. Burley* [c], *Steven L. Neale* [a], *and Alasdair W. Clark** [a]

[a] School of Engineering, University of Glasgow, Rankine Building, Oakfield Avenue, Glasgow, UK. E-mail: Alasdair.clark@glasgow.ac.uk

[b] School of Chemistry, University of Glasgow, Joseph Black Building, Glasgow, UK, G12 8QQ.

[c] WestCHEM & Department of Pure & Applied Chemistry, University of Strathclyde, 295 Cathedral Street, Glasgow, G1 1XL, UK. E-mail: glenn.burley@strath.ac.uk

‡ These authors contributed equally to this work

** Corresponding author: Alasdair.Clark@glasgow.ac.uk*

Keywords: LSPR, plasmonics, optical tongue, sensor array, sensors, pattern-recognition

S1. Determination of Periodicity

For optimization of the periodicity between the Al and Au nanostructure arrays (**Figure S1a**), finite-difference time-domain (FDTD) simulations were conducted using Lumerical. A linearly polarized plane wave was defined for a unit area cell with various periods (**Figure S1b**). The dielectric values of Au and titanium were obtained from the CRC library, [1] and the dielectric values of glass and Al were obtained from the Palik library. [2] Periodic boundary conditions were used in the X-axis and Y-axis, and a perfectly-matched-layers (PML) boundary was used in the Z-axis. A uniform mesh size of 4 nm was used in all axes and the background refractive index (RI) was set to that of water (RI=1.333).

Based on the simulation results, a period of 300 nm for each array (offset by 150 nm in X and Y) was chosen for fabrication of this proof-of-concept device because it provides for two distinct peaks with the highest transmission attenuation with virtually no coupling between the two nanostructures at their resonance peaks (**Figure S1c**).

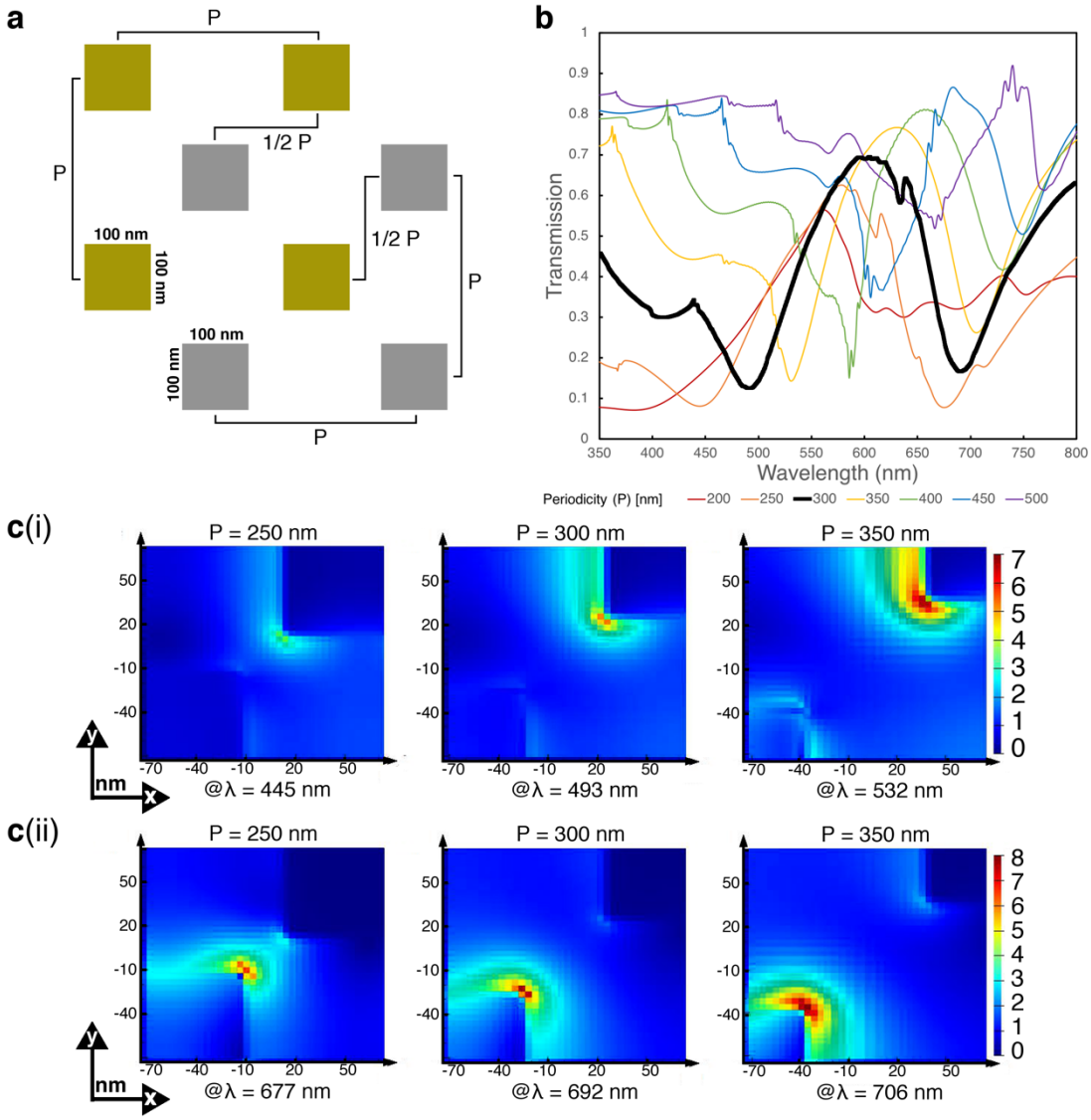

Figure S1: FDTD simulation of different periodicities between Al and Au nanostructures in bimetallic arrays. (a) *Rendering of the simulation of the effect of periodicity (P) for arrays of Au and Al nanostructures with dimensions of 100 x 100 x 50 nm (length x width x height). For each simulation, the nanostructures were considered to be offset by half a period in both X and Y.* ***(b)*** *Resulting transmission as P increases from 200 nm to 500 nm, in increments of 50 nm.* ***(c)*** *The XY electric field between the nanostructures for a wavelength corresponding to* ***(i)*** *Resonance 1 (Al) and* ***(ii)*** *Resonance 2 (Au) from (b) (as labelled below each subfigure) for P of 250 nm, 300 nm, and 350 nm. As indicated by the bold line in (b) and the middle electric field plots of c(i) and c(ii), P = 300 nm shows two distinct peaks, with high transmission, and virtually no coupling between the nanostructures at their resonance peaks.*

S2. Fabrication and Alignment

SEM images of two monometallic (top row) and ten bimetallic (bottom two rows) nanostructure arrays are shown in **Figure S2**. The two metals can be differentiated by the shade of grey due to their distinct electron scattering properties, Au being 'brighter' and Al being 'darker.' [3] While the bimetallic sensors were written with the same programmed pattern alignment, variations in alignment between the two metallic arrays within each region is clearly visible. This variation in alignment can cause the two metal arrays to become within close proximity with one another and produce coupling effects on the resonance peaks for each metal.

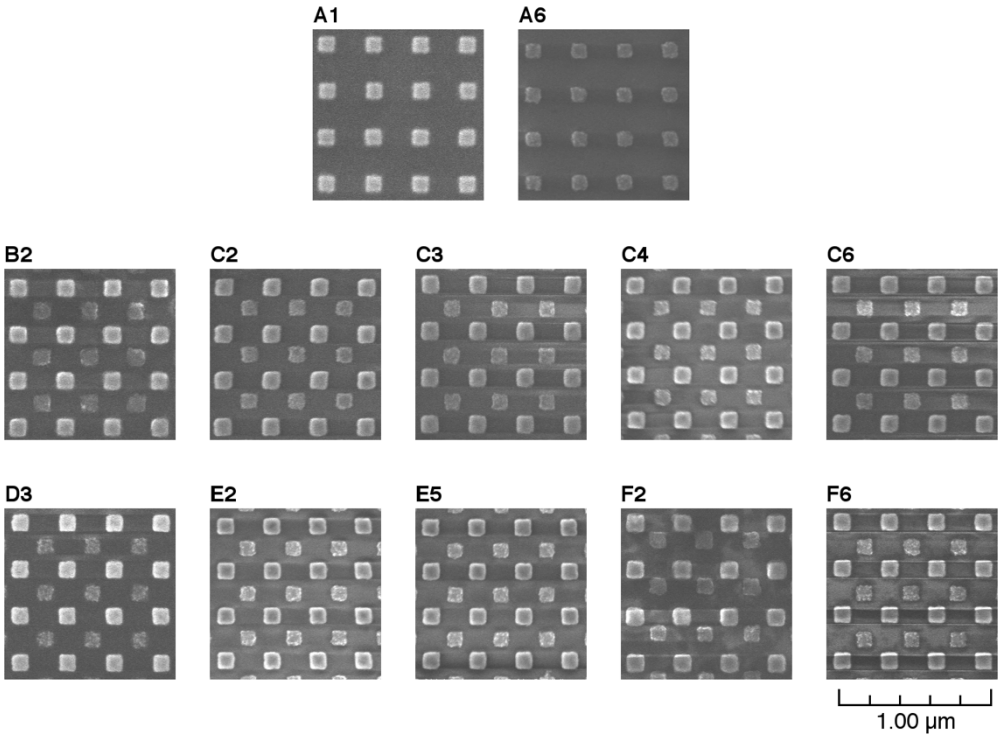

Figure S2: SEM of 12 Sensors. *Sensors A1 and A6 are control regions of Au and Al, respectively. Sensors B2, C2, C3, C4, C6, D3, E2, E5, F2, and F6 are all bimetallic Au/Al sensors. For each bimetallic SEM, the outer 4x4 array is Au and the offset, inner 3x3 array is of Al. Although the alignment between the two metal arrays is within fabrication tolerance of the e-beam lithography tool, there is a slight difference in the alignment between each metallic array in each bimetallic sensor.*

S3. Effect of Al-Au Nanostructure Distance for Bimetallic Array

To understand the effects of alignment during fabrication on the electric field between the nanostructures, FDTD simulation using Lumerical was carried out. A linearly polarized plane wave was defined for a unit area cell with a period of 300 nm in both X and Y. Both nanostructures were defined with dimensions of 100 nm x 100 nm x 50 nm (length by width by height). The distance between the Au and Al nanostructures was decreased from largest distance possible between structures (150 nm in X and Y for a period of 300 nm) to 'touching,' as shown in **Figure S3a**. The dielectric values of Au and titanium were obtained from the CRC library, [1] and the dielectric values of glass and Al were obtained from the Palik library. [2] Periodic boundary conditions were used in the X-axis and Y-axis, and a perfectly-matched-layers (PML) boundary was used in the Z-axis. A uniform mesh size of 4 nm was used in all axes and the background refractive index (RI) was set to that of water (RI=1.333).

As seen by the resulting electric field at the resonance associated with Al (**Figure S3b**) and Au (**Figure S3c**), strong coupling occurs when the alignment between nanostructure arrays is off by more than 25 nm (iii-v).

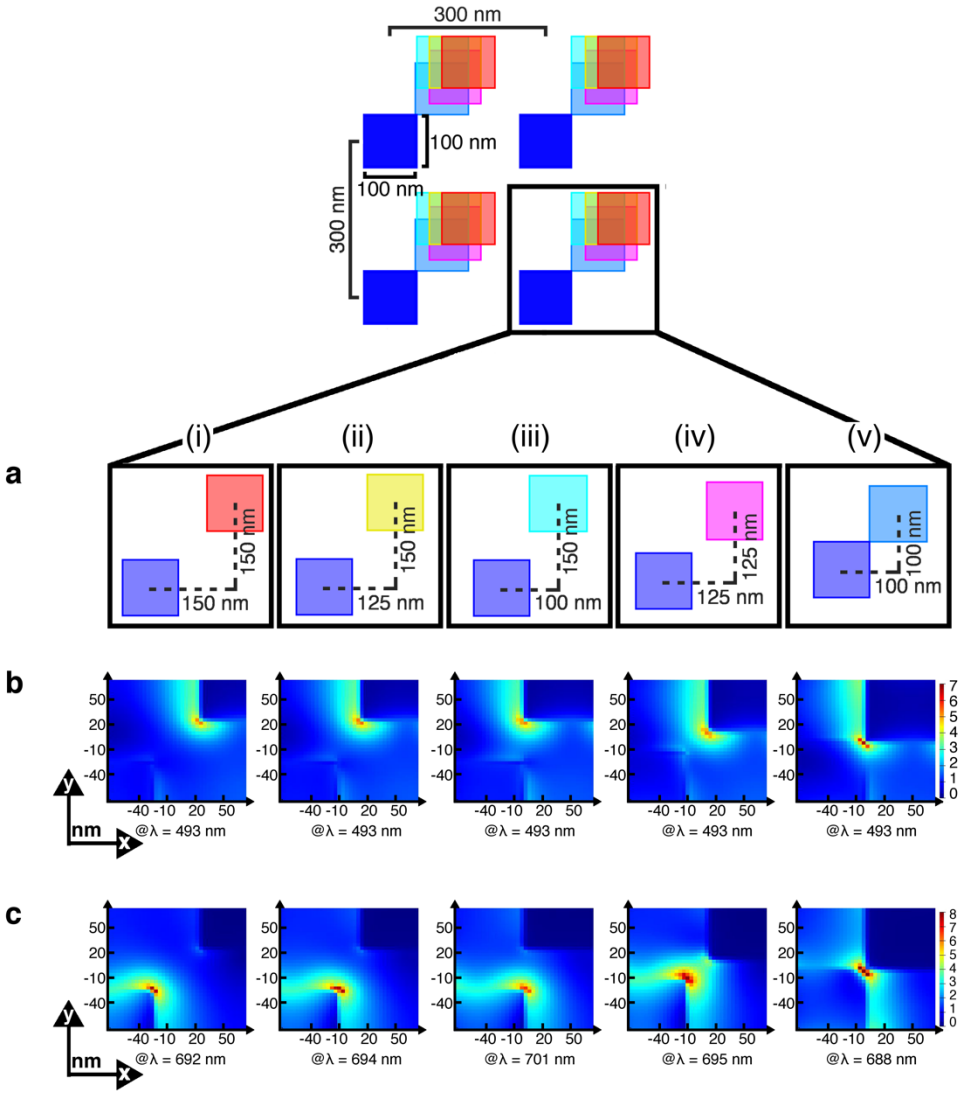

Figure S3: FDTD simulation of effect on electric field by changes to distance between Al and Au nanostructures in a bimetallic array. (a) *Rendering of the simulations and resulting XY electric fields for the resonance peaks corresponding to* ***(b)*** *Al and* ***(c)*** *Au as the distance between the metal nanostructures is decreased. Simulation for nanostructures separated in (X, Y) by* ***(i)*** *(150 nm, 150 nm),* ***(ii)*** *(125 nm, 150 nm),* ***(iii)*** *(100 nm, 150 nm),* ***(iv)*** *(125 nm, 125 nm), and* ***(v)*** *(100 nm, 100 nm) are shown. The nanostructures of Au and Al are 100 nm x 100 nm x 50 nm (length x width x height) with an X-Y period of 300 nm between each Au-Al pair and a mesh size of 4 nm in X-Y-Z was used. The resulting electric fields indicate strong coupling when alignment is off by more than 25 nm in either X or Y.*

S4. Effect of Surface Chemistries on Transmission Resonance

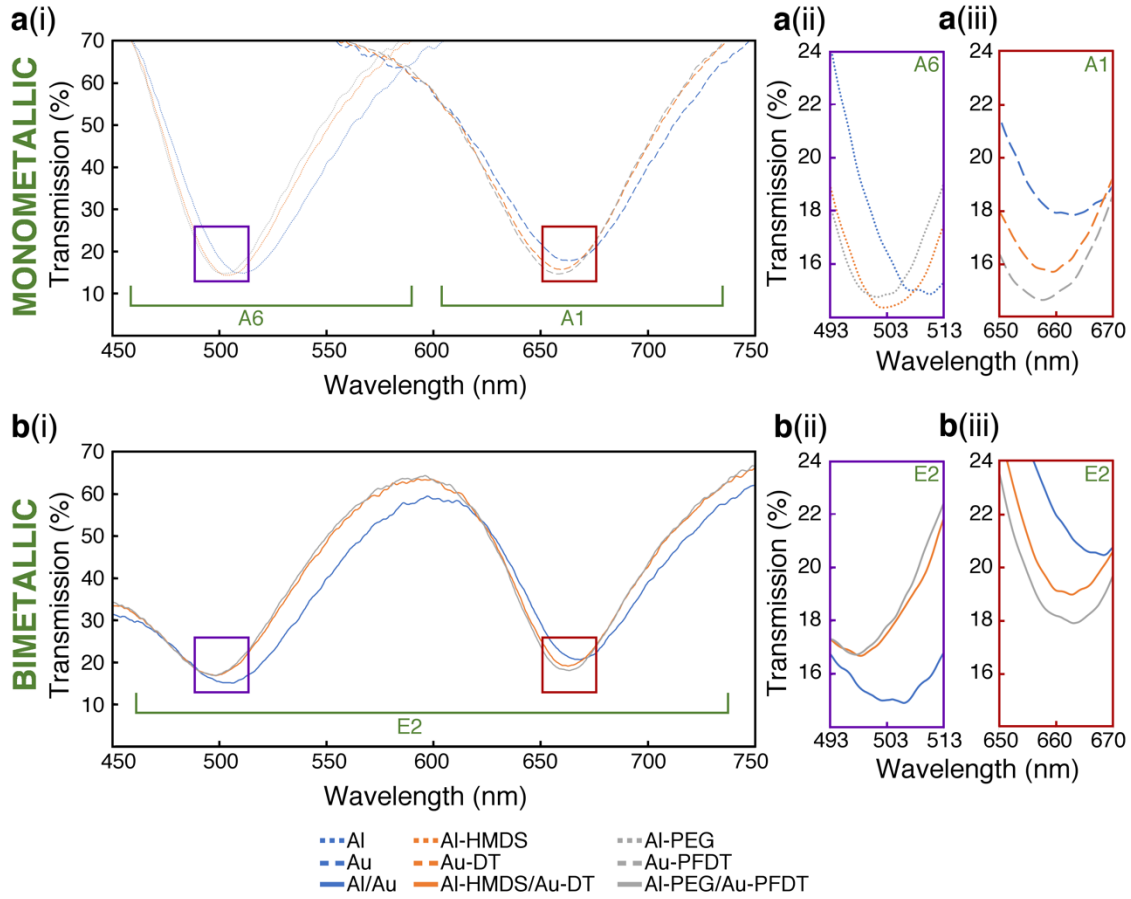

Figure S4: The effect of surface chemistry on transmission response. *The transmission response in water from* ***(a)*** *six monometallic sensors (Al, Au, Al-HMDS, AU-DT, Al-PEG, and Au-PFDT) and* ***(b)*** *three bimetallic sensors (Al/Au, Al-HMDS/Au-DT, and Al-PEG/Au-PFDT) for the wavelength ranges of (i) 450 nm to 750 nm, (ii) 493 nm to 513 nm (a zoom-in corresponding to the Al-type nanostructure peaks), and (iii) 650 nm to 670 nm (a zoom-in corresponding to the Au-type nanostructure peaks). Both the surface chemistry present on the metallic nanostructures and the type of sensor (mono- versus bimetallic) results in unique transmission responses.*

S5. Data Matrix for Analysis

The matrix for both organic solvent differentiation and whisky differentiation are derived from a *N* x *R* matrix, where the *N* rows correspond to a given solution, and the *R* columns correspond to the solution tested and the transmission peak response of Al, Au, Al-HMDS, Au-DT, Al-PEG, and Au-PFDT to that given solution. An example is given in **Table S1** below.

Table S1: Example table of the data analyzed by PCA and LDA for organic solvent differentiation and whisky differentiation.

	Transmission Peak Response (nm)					
Solution	**Al**	**Au**	**Al-HMDS**	**Au-DT**	**Al-PEG**	**Au-PFDT**
Solution 1	*492.79*	*660.17*	*485.49*	*661.4*	*484.11*	*659.04*
Solution 2	*494.03*	*663.36*	*488.69*	*664.59*	*486.19*	*661.61*
			. . .			
Solution N	*495.14*	*664.75*	*490.01*	*664.32*	*485.54*	*661.51*

For PCA analysis, the data matrix is transformed to a new *N* x *R* matrix, where the *N* rows correspond to the solutions in the same order as they appear in the initial matrix, and the *R* columns correspond to the six variables called principal components (PC). Each PC is derived from linear combinations of the transmission peaks (R) of each of the metallic regions from the initial data matrix, using mathematically derived coefficients (a, b, c, d, e, f) that result in a maximization of variance along each component:

$$PC_1 = a_1 \cdot R_{Al} + b_1 \cdot R_{Au} + c_1 \cdot R_{Al\_HMDS} + d_1 \cdot R_{Au\_DT} + e_1 \cdot R_{Al\_PEG69} + f_1 \cdot R_{Au\_PFDT}$$
$$PC_2 = a_2 \cdot R_{Al} + b_2 \cdot R_{Au} + c_2 \cdot R_{Al\_HMDS} + d_2 \cdot R_{Au\_DT} + e_2 \cdot R_{Al\_PEG69} + f_2 \cdot R_{Au\_PFDT}$$
$$\vdots$$
$$PC_6 = a_6 \cdot R_{Al} + b_6 \cdot R_{Au} + c_6 \cdot R_{Al\_HMDS} + d_6 \cdot R_{Au\_DT} + e_6 \cdot R_{Al\_PEG69} + f_6 \cdot R_{Au\_PFDT}$$

where PC_1 describes the most variance of the data and PC_6 describes the least.

S6. PCA for Acetone and Ethanol: Monometallic and Bimetallic Arrays

Figure S5 shows the PCA result from modifying the refractive index using 10%, 20%, and 30% solutions of acetone and ethanol for **(a)** monometallic Al and Au arrays (elements A1 and A6 from **Figure S5**) and **(b)** bimetallic arrays (element E2 from **Figure S5**). For both the monometallic and bimetal sensor arrays, the PCA for **(i)** Al and Au, only; **(ii)** Al, Au, Al-HMDS, and Au-DT; and **(iii)** Al, Au, Al-HMDS, Au-DT, Al-PEG, and Au-PFDT are shown. In each PCA, black dots represent DI water, red dots represent acetone-based media and yellow dots represent ethanol-based media.

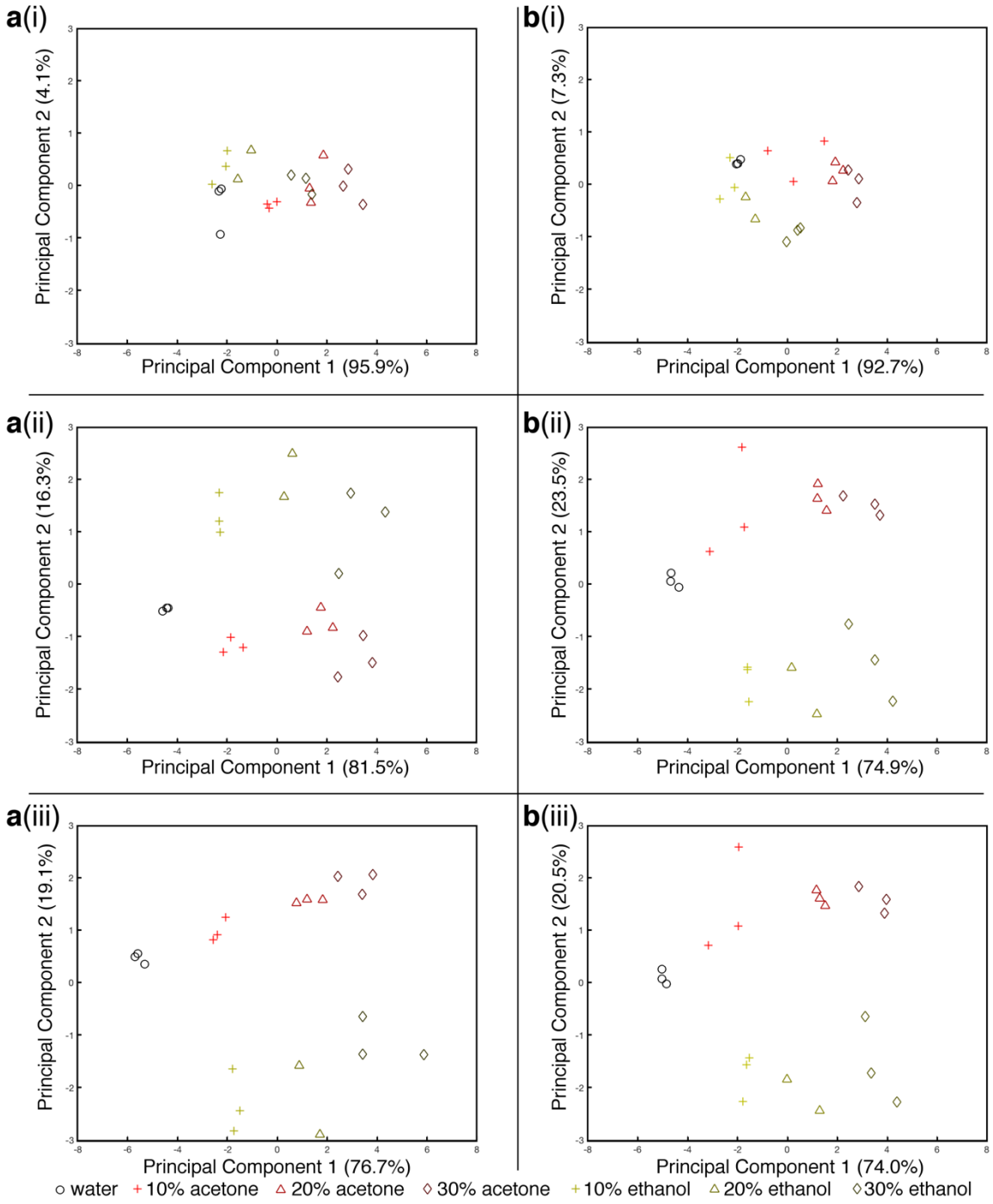

Figure S5: 2D PCA for organic solvent differentiation using mono- and bimetallic sensor arrays. *This figure shows plots of the first and second principal components (2D PCA) of the plasmonic peaks from an optical-tongue sensor consisting of* ***(a)*** *monometallic Au and Al arrays (elements A1/A6) and* ***(b)*** *bimetallic arrays of Au and Al (element E2). For both the monometallic and bimetallic arrays of sensors, the 2D PCA of* ***(i)*** *Al and Au, only;* ***(ii)*** *Al, Au, Al-HMDS, and Au-DT; and* ***(iii)*** *Al, Au, Al-HMDS, Au-DT, Al-PEG, and Au-PFDT are shown. As more elements are added to the PCA, the optical tongue is better able to distinguish the difference between water and 10%, 20%, and 30% (v/v) acetone and ethanol. This works for both the optical-tongue consisting of 6 monometallic arrays and that of 3 bimetallic arrays. The bimetallic optical-tongue is therefore able to differentiate between these organic solvents while being only half the size compared to the monometallic one.*

As more elements to the sensor array are added to the PCA, further differentiation between classes immerge, which is indicated by the further separation of groupings. The PCA of the first three principal components for all six chemistries is shown in **Figure S6**.

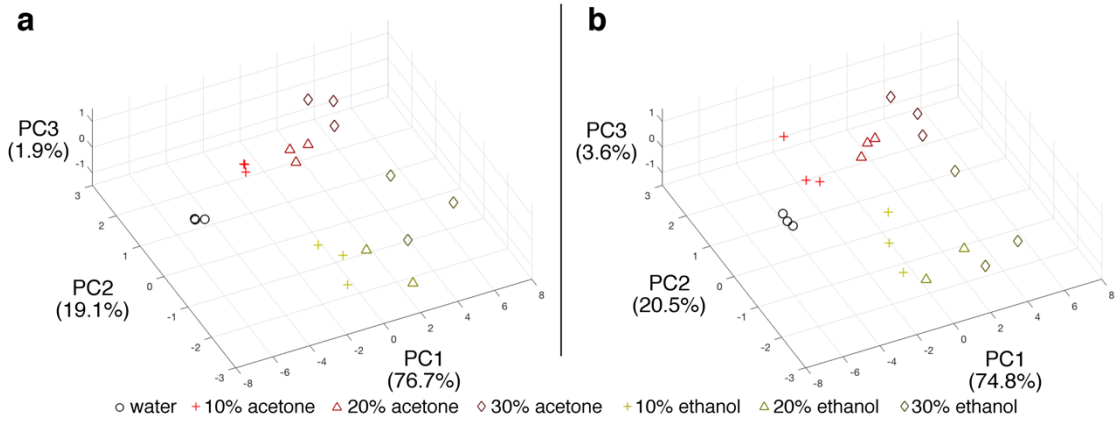

Figure S6: 3D Principal Component Analysis (PCA) for organic solvent differentiation. *Plot of the first (PCA1), second (PCA2), and third (PCA3) principal components of organic solvent sensing for* ***(a)*** *monometallic and* ***(b)*** *bimetallic sensor arrays from* ***Figure S5a(iii)*** *and* ***Figure S5b(iii)****. The third component further helps differentiate sensing of the organic solvents.*

S7. PCA for Whisky Tongue: Monometallic and Bimetallic Arrays

Figure S7a shows the transmission response of the Al/Au element of the bimetallic sensor to water (blue), vodka (orange), and W1 (grey) with zoomed in transmission response at the peaks corresponding to Al (**Figure S7b(i)**) and Au (**Figure S7b(ii)**). These peak positions were used for data analysis as described in Table S1.

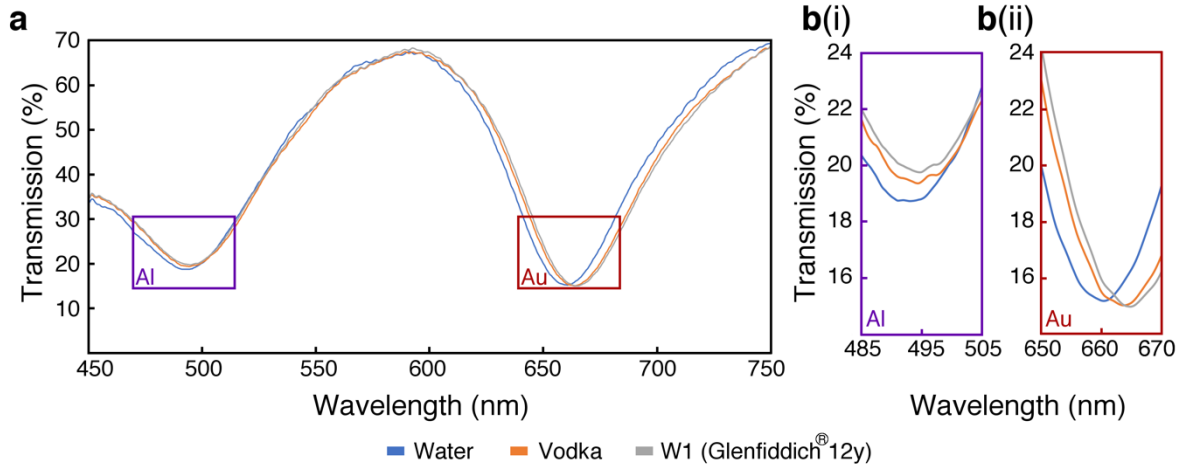

Figure S7: Example of the (a) transmission response of the Al/Au element in the whisky tongue array to water, vodka, and W1, with (b) zoomed-in plots corresponding to (i) Al and (ii) Au peaks. *A different shift in peak position from water for both vodka and W1 in the regions corresponding to Al and Au can be seen.*

The resulting PCA for the first two principal components for monometallic (elements A1 and A6 from **Figure S2**) and bimetallic (element E2 from **Figure S2**) sensing arrays are shown in **Figure S8a** and **Figure S8b**, respectively. The colours and symbols used in the PCA are identified by the first column of **Table S2**. For both the mono- and bimetallic arrays of sensors, the PCA for chemistries of **(i)** Al and Au, only; **(ii)** Al, Au, Al-HMDS, and Au-DT; and **(iii)** Al, Au, Al-HMDS, Au-DT, Al-PEG, and Au-PFDT are shown. Similar to the organic solvent tests, further differentiation is achieved as more elements are added to the PCA. The boxed region in (iii), which contains the alcohol solutions, is enlarged in **(iv)**.

Table S2: Alcohols tested in the whisky tongue.

ID	Name	Serial Number	%	Type	Region	Barrel	Malt	Age
0 ○	DI H_2O	-	0	Deionised Water	-	-	-	-
E ○	40% Ethanol in DI H_2O (v/v)	-	40	Deionised Water / Ethanol Mixture	-	-	-	-
V ◇	Absolut	L20180109H 16:07	40	Vodka	-	-	-	-
W1 +	Glenfiddich® 12 y	L33B46542108 0841	40	Scotch Whisky	Speyside	Amer. Oak / Eur. Sherry	Single	12
W2 Δ	Glenfiddich® 15 y	L33B44663005 1142	40	Scotch Whisky	Speyside	Eur. Sherry / Solera Vat	Single	15
W3 ◇	Glenfiddich® 18 y	L33B46271907 1531	40	Scotch Whisky	Speyside	Amer. Oak / Span. Oloroso	Single	18
W4 +	Glen Marnoch® Sherry Cask	LBB6B1406 021117 15:44	40	Scotch Whisky	Highland	Amer. Oak / Eur. Sherry	Single	-
W5 Δ	Glen Marnoch® Bourbon Cask	LBB6B1405 021117 19:42	40	Scotch Whisky	Highland	Amer. Oak / Bourbon	Single	-
W6 ◇	Glen Marnoch® Rum Cask	LBB6B1407 021117 17:53	40	Scotch Whisky	Highland	Amer. Oak / Caribbean Rum	Single	-
W7 ◇	Laphroaig® 10 y	L6262MB2 22990853	40	Scotch Whisky	Islay	Bourbon	Single	10

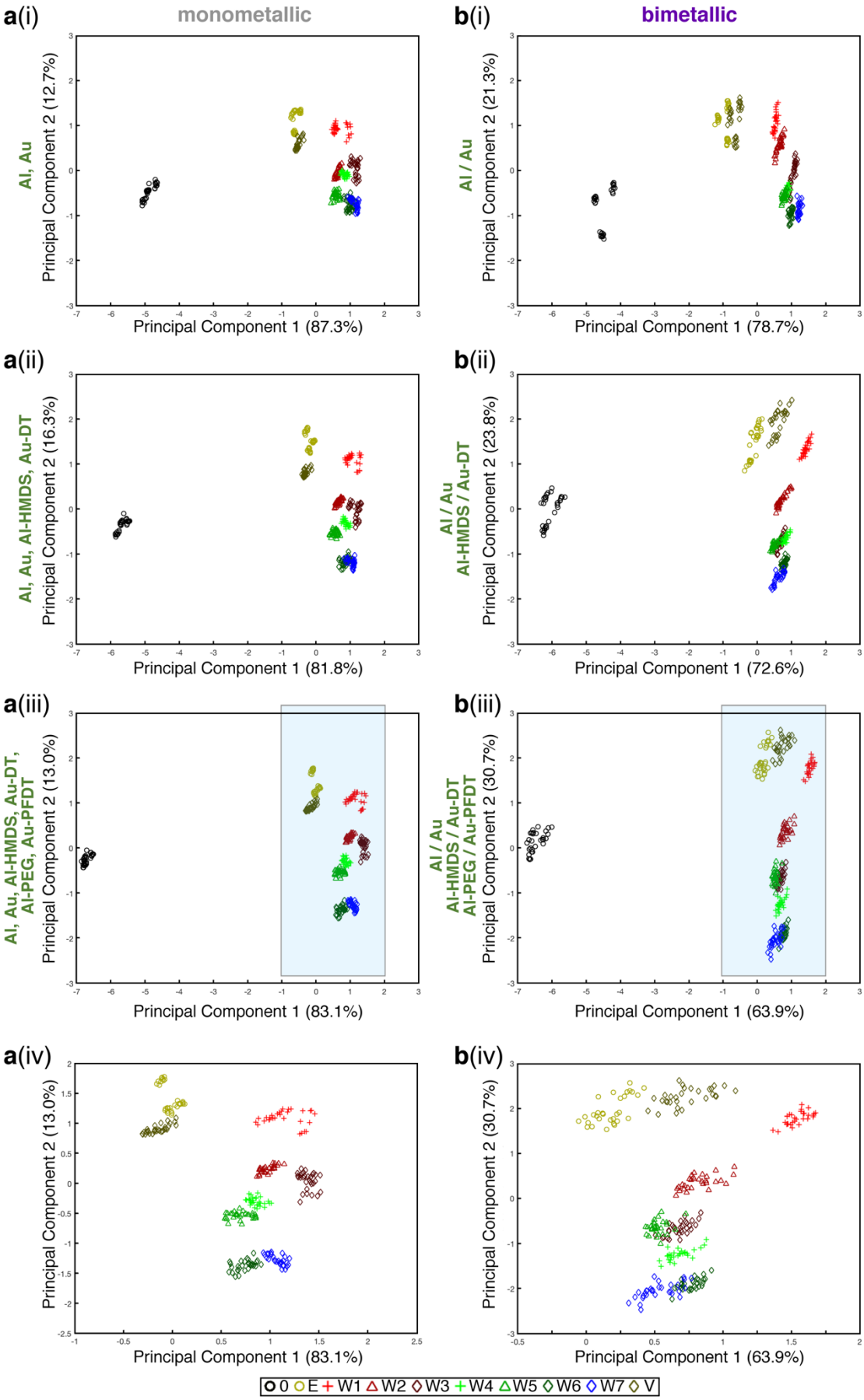
a(i)
monometallic
b(i)
bimetallic
Al, Au
Principal Component 2 (12.7%)
Principal Component 1 (87.3%)
Al / Au
Principal Component 2 (21.3%)
Principal Component 1 (78.7%)
a(ii)
b(ii)
Al, Au, Al-HMDS, Au-DT
Principal Component 2 (16.3%)
Principal Component 1 (81.8%)
Al / Au
Al-HMDS / Au-DT
Principal Component 2 (23.8%)
Principal Component 1 (72.6%)
a(iii)
b(iii)
Al, Au, Al-HMDS, Au-DT,
Al-PEG, Au-PFDT
Principal Component 2 (13.0%)
Principal Component 1 (83.1%)
Al / Au
Al-HMDS / Au-DT
Al-PEG / Au-PFDT
Principal Component 2 (30.7%)
Principal Component 1 (63.9%)
a(iv)
b(iv)
Principal Component 2 (13.0%)
Principal Component 1 (83.1%)
Principal Component 2 (30.7%)
Principal Component 1 (63.9%)
0 E W1 W2 W3 W4 W5 W6 W7 V

Figure S8: 2D PCA for whisky differentiation. *This figure shows plots of the first and second principal components of the plasmonic peaks from an optical-tongue sensor consisting of* ***(a)*** *monometallic Au and Al arrays (elements A1/A6 from* ***Figure S2****) and* ***(b)*** *bimetallic arrays of Au and Al (element E2 from* ***Figure S2****).* ***(i-iii)*** *2D PCA of (i) native chemistries, only; (ii) native chemistries, Au-DT, and Al-HMDS; and (iii) native chemistries, Au-DT, Al-HMDS, Au-PFDT, and Al-PEG.* ***(iv)*** *Zoomed in plot of the box from (iii) to show more closely the PCA region containing the tested alcoholic solutions. For identification of the solutions, the colors of and symbols correspond to Column 1 of* ***Table S2****.*

To further exhibit the achieved differentiation, the first, second, and third principal components for all chemistries (as shown in **Figure S8a(iii)** and **Figure S8b(iii)**, representing >95% variance) are shown in **Figure S9** for the **(a)** mono- and **(b)** bimetallic arrays. The inset in each figure shows a magnified view of the region of the PCA containing only the alcohol elements.

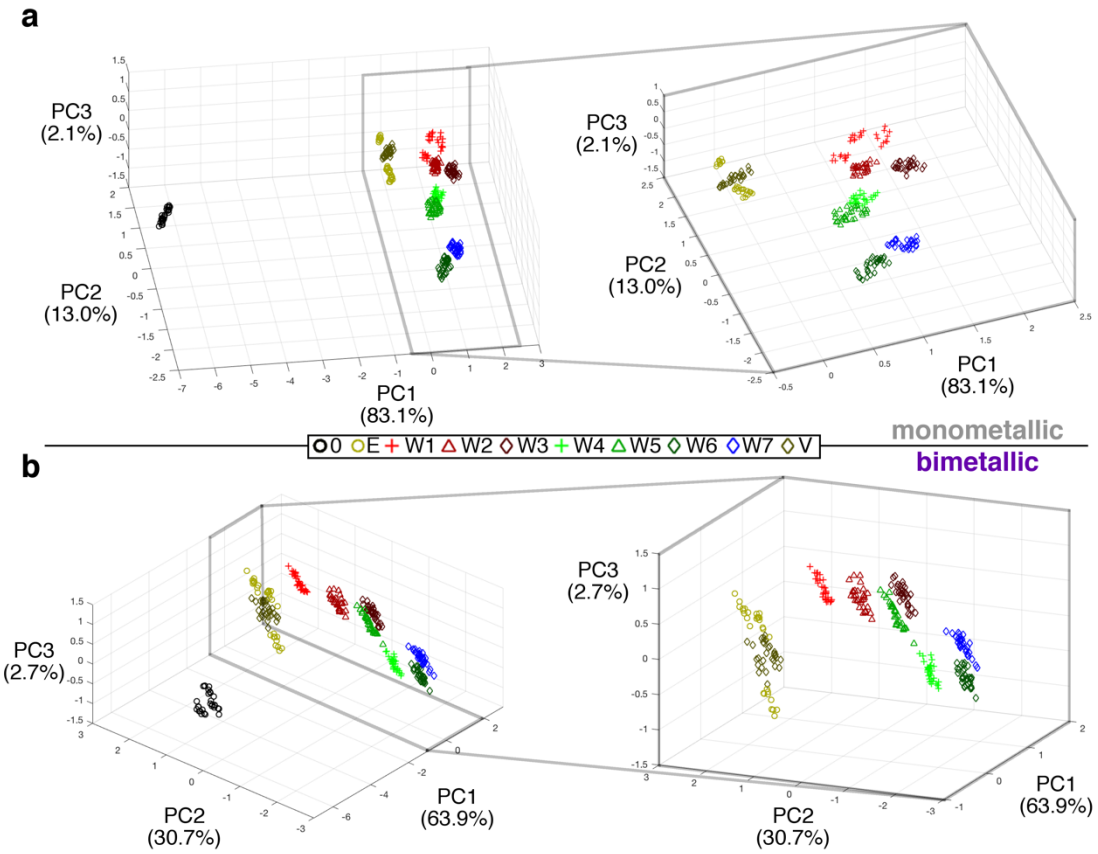

Figure S9: 3D PCA for whisky differentiation. *The PCA of optical-tongue arrays with* ***(a)*** *6 monometallic and* ***(b)*** *3 bimetallic sensing regions for the differentiation of the solutions in Table S2.* ***(right)*** *Zoomed in plot of the box indicated in the corresponding PCA to the left, showing the differentiation of the whiskies.*

The resulting coefficients (see **Data Matrix for PCA Analysis** above) for the first (PC1), second (PC2), and third (PC3) principal components for the monometallic (A1/A6) and

bimetallic (E2) whisky tongues are shown in **Table S3**. These PCs are derived from using the full transmission peak response matrix for the monometallic and bimetallic tongues (i.e. all 6 regions in the monometallic tongue and all 3 regions in the bimetallic tongue).

Table S3: Coefficients for the first, second, and third principal components of the monometallic and bimetallic whisky tongues (using the full tongue arrays consisting of all 6 and all 3 sensing regions, respectively).

	PC	*Al*	*Au*	*Al-HMDS*	*Au-DT*	*Al-PEG*	*Au-PFDT*	% variance
monometallic (A1/A6)	*1*	0.341	0.667	0.213	0.349	0.325	0.407	*83.1*
	2	0.515	-0.568	0.582	0.019	0.269	-0.034	*13.0*
	3	-0.236	0.223	0.081	-0.437	0.725	-0.414	*2.1*
bimetallic (E2)	*1*	0.215	0.673	0.474	0.397	0.088	0.333	*63.9*
	2	0.454	-0.467	0.390	-0.015	0.648	-0.057	*30.7*
	3	0.087	0.473	-0.531	-0.367	0.593	0.024	*2.7*

For the monometallic tongue, the most weight in PC1 is attributed to the transmission response of Au then Au-PFDT and for the bimetallic, Au then Al-HMDS. For PC2, the most weight for the monometallic tongue is attributed to the transmission response of Al-HMDS, and for the bimetallic is attributed to the response of Al-PEG. The difference in the order of weights of each element in the sensing array for the mono- and bimetallic tongues indicates there is an influence of combining the two metallic nanostructures in one region that thus effects sensitivity.

S8. LDA for Whisky Tongue: Monometallic and Bimetallic Arrays

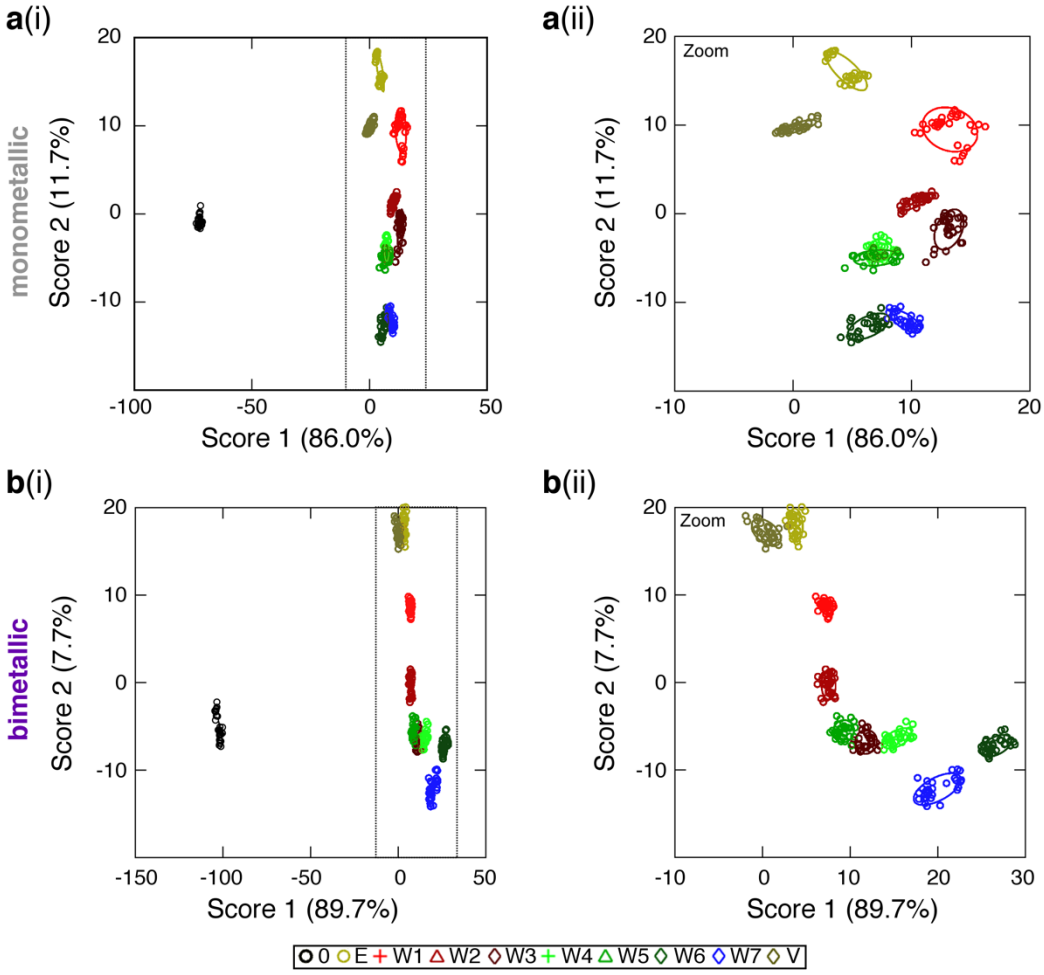

Figure S10: LDA classification of whisky using (a) mono- and (b) bimetallic tongue devices. *For both analyses, (i) shows the full LDA and (ii) shows a zoomed in LDA of only the alcoholic solutions. For the monometallic device, classification had 100% accuracy. W4 and W5 are well separated in Score 3 (1.1%). For the bimetallic device, classification had 99.7% accuracy (W3 and W5 had one point misclassified). W4 is well separated out by Score 3 (1.9%). The ellipses are one standard deviation.*

References

(1) Rumble, J. R.; Lide, D. R.; Bruno, T. J. *CRC Handbook of Chemistry & Physics*, 98 ed.; CRC Press: Boca Raton, USA, 2017.

(2) Palik, E. D. *Handbook of Optical Constants of Solids*, Academic Press: 1997; Vol. I-III.

(3) Goldstein, J. I.; Newbury, D. E.; Micheal, J. R.; Ritchie, N. W. M.; Scott, J. H. J.; Joy, D. C. *Scanning Electron Microscopy and X-Ray Microanalysis*, 4 ed.; Springer: 2017.